Joint inversion of full-waveform GPR and ER data enhanced by the envelope transform and cross-gradients

Diego Domenzain, Colorado School of Mines; John Bradford, Colorado School of Mines; Jodi Mead, Boise State University*

SUMMARY

Full-waveform inversion (FWI) of surface acquired GPR data can be prone to non-uniqueness and poor resolution of the recovered parameters when low frequency information is missing in the data. We present a novel non-linear joint inversion of GPR and electrical resistivity (ER) data that enhances long wavelength and accuracy in the recovered electrical permittivity and conductivity of the subsurface. We do so by (i) exploiting the inherent link of GPR and ER data to conductivity given by Maxwell's equations, (ii) using the envelope of the GPR data in the FWI scheme, and (iii) iteratively implementing the cross-gradients constraint directly in the inversion. Our scheme improves the accuracy, frequency content, and depth resolution of the permittivity and conductivity solutions compared to individual GPR and ER inversions.

INTRODUCTION

FWI of surface acquired GPR data can be prone to non-uniqueness and poor resolution of the recovered parameters when low frequency information is missing in the data (Pratt et al., 1998; Meles et al., 2012; Lavoué et al., 2014). In contrast to GPR data, electrical resistivity (ER) data is directly sensitive to electrical conductivity at longer wavelengths. In Domenzain et al. (2018) and Domenzain et al. (2019a) the authors show that ER data improves the accuracy and low frequency content of the conductivity solution.

Our algorithm assumes the DC conductivity to which ER is sensitive to, equals the effective conductivity to which the GPR is sensitive to. Although frequency independent parameters are genrally not true in nature, this approximation holds within an order of magnitude for most earth materials (see Table 1).

	Effective (mS/m)	DC (mS/m)	Effective/DC
Dry sand	4.54	0.45	10.1
Moist sand	6.53	2	3.26
Wet sand	8.06	6.06	1.33
Silty loam	17.3	3.5	4.93
Humus	43.1	19.5	2.21
Laterite	45	9	5
Wet clay	68.4	42.5	1.61
Loess	185	72.3	2.55

Table 1: Frequency dependent and DC conductivities at 250MHz given by the Cole-Cole model with relaxation parameters from Taherian et al. (1990); Friel and Or (1999) and Bradford (2007). Most earth materials present an increase of at most 5 between DC and (real) effective conductivity.

We present a novel non-linear 2D joint inversion of GPR and ER data that enhances spatial-frequency content and accuracy in the recovered electrical permittivity and conductivity of the subsurface. We do so by

1. using the envelope of the GPR data in the FWI scheme,
2. iteratively using structural constraints (via cross-gradients) that exploit the different spatial-frequency sensitivities both parameters have,
3. exploiting the inherent link of GPR and ER data to conductivity given by Maxwell's equations.

In Bozdağ et al. (2011) and Liu and Zhang (2017) the authors use the envelope of seismic waveforms in a FWI scheme to enhance low frequency content. In this work, we use the envelope of the GPR data in order to improve longer wavelength resolution and accuracy at depth of both permittivity and conductivity.

In Haber and Oldenburg (1997) and Gallardo and Meju (2003) the authors use structural constraints on the recovered parameter by joining the sensitivities of two different geophysical methods. In this work, we use structural constraints on the recovered electrical permittivity and conductivity. We are able to inform both parameters of their missing spatial-frequency content - permittivity lacks low and conductivity lacks high spatial-frequencies.

By joining the sensitivities of the GPR and ER data in the optimization, we completely relax the need for external regularization. However, a smooth initial model for both permittivity and conductivity is needed for satisfactory convergence.

OPTIMIZATION

Our objective function takes the form of,

$$\begin{aligned}\{\boldsymbol{\varepsilon}_*, \boldsymbol{\sigma}_*\} = \arg\min\ & \tilde{\Theta}_w(\boldsymbol{\varepsilon}, \boldsymbol{\sigma}; \mathbf{d}_w^o, \mathbf{d}_{w,a}^o) + \\ & \Theta_\tau(\boldsymbol{\varepsilon}, \boldsymbol{\sigma}) + \\ & \Theta_{dc}(\boldsymbol{\sigma}; \mathbf{d}_{dc}^o).\end{aligned} \tag{1}$$

where $\tilde{\Theta}_w$, Θ_τ and Θ_{dc} are the sum squared errors of the GPR data and its envelope, the cross-gradient constraint, and the ER data respectively. The GPR and ER observed data are denoted by $\mathbf{d}_w^o$ and $\mathbf{d}_{dc}^o$ respectively. The relative permittivity and conductivity are denoted by $\boldsymbol{\varepsilon}$ and $\boldsymbol{\sigma}$.

In the following sections we explain our algorithm only for $\boldsymbol{\sigma}$. The procedure for $\boldsymbol{\varepsilon}$ is analogous except Θ_{dc} is not used since the ER experiment is not sensitive to $\boldsymbol{\varepsilon}$.

Envelope of GPR data

The objective function of only the GPR data is,

$$\tilde{\Theta}_w = \Theta_w(\boldsymbol{\varepsilon}, \boldsymbol{\sigma}; \mathbf{d}^o_w) + \Theta_{w,a}(\boldsymbol{\varepsilon}, \boldsymbol{\sigma}; \mathbf{d}^o_{w,a}), \tag{2}$$

where Θ_w and $\Theta_{w,a}$ denote the sum squared errors of the data and the envelope of the data respectively. By adding $\Theta_{w,a}$ we enhance the low frequency content of the GPR data. We compute the gradients $\mathbf{g}_{w,\sigma}$ and $\mathbf{g}_{\sigma,a}$ of Θ_w and $\Theta_{w,a}$ respectivley using a time domain FWI approach (Domenzain et al., 2019b).

Cross-gradients constraint

The cross-gradients constraint is given by minimizing the objective function,

$$\begin{aligned} \Theta_\tau(\boldsymbol{\varepsilon}, \boldsymbol{\sigma}) &= \frac{1}{2}||\tau||_2^2, \\ \tau(\boldsymbol{\varepsilon}, \boldsymbol{\sigma}) &= \nabla_{\mathbf{x}} \boldsymbol{\varepsilon} \times \nabla_{\mathbf{x}} \boldsymbol{\sigma}, \end{aligned} \tag{3}$$

where $\nabla_{\mathbf{x}}$ denotes the spatial gradient in the xz-plane.

At each iteration of our algorithm, we optimize equation 3 using Gauss-Newton,

$$\Delta\boldsymbol{\sigma}_\tau = -(\mathbf{J}_{\tau,\sigma}\mathbf{J}^\top_{\tau,\sigma} + \alpha_{\tau,\sigma}\mathbf{I})^{-1} \cdot (\mathbf{J}_{\tau,\sigma}\,\tau), \tag{4}$$

where $\mathbf{J}_{\tau,\sigma}$ is the Jacobian of τ with respect to σ.

Our approach differs from the original formulation of cross-gradients (Gallardo and Meju, 2003) in that we can allow one of the parameters to remain fixed while Θ_τ is optimized (see Figure 1 for an example). This enables our algorithm to enforce the structure of either parameter over the other. In order to achieve this, we stack the updates $\Delta\boldsymbol{\sigma}_\tau$ during the optimization of Θ_τ,

$$\Delta\boldsymbol{\sigma}_{\tau,\circ} \leftarrow \Delta\boldsymbol{\sigma}_{\tau,\circ} + \Delta\boldsymbol{\sigma}_\tau. \tag{5}$$

After normalizing $\Delta\boldsymbol{\sigma}_\tau$ by its largest magnitude, we scale by a real number b_σ,

$$\Delta\boldsymbol{\sigma}_{\tau,\circ} \leftarrow b_\sigma\,\Delta\boldsymbol{\sigma}_{\tau,\circ}. \tag{6}$$

The weight b_σ increases throughout iterations as the parameters are better resolved. See Figure 2 for a qualitative diagram.

Envelope, cross-gradients and ER data

We optimize equation 1 by first computing the gradients $\tilde{\mathbf{g}}_\sigma$ and $\mathbf{g}_{dc}$ of $\tilde{\Theta}_w$ and Θ_{dc} respectively, and then adding the cross-gradients update $\Delta\boldsymbol{\sigma}_{\tau,\circ}$,

$$\begin{aligned} \tilde{\mathbf{g}}_\sigma &\leftarrow \mathbf{g}_{w,\sigma} + \beta_\sigma\,\mathbf{g}_{\sigma,a} + \Delta\boldsymbol{\sigma}_{\tau,\circ}, \\ \mathbf{g}_{dc} &\leftarrow \mathbf{g}_{dc} + \Delta\boldsymbol{\sigma}_{\tau,\circ}. \end{aligned} \tag{7}$$

The gradient $\mathbf{g}_{dc}$ is computed using the adjoint method (Domenzain et al., 2018, 2019a). All gradients are calculated in the same computational grid.

We repeat this process for each source in our survey and write the updates for the conductivity as,

$$\Delta\boldsymbol{\sigma}_w = -\frac{1}{n_w}\sum_{s=1}^{n_w}\alpha_\sigma\,\tilde{\mathbf{g}}_\sigma, \tag{8}$$

$$\Delta\boldsymbol{\sigma}_{dc} = -\frac{1}{n_{dc}}\sum_{s=1}^{n_{dc}}\alpha_{dc}\,\mathbf{g}_{dc}, \tag{9}$$

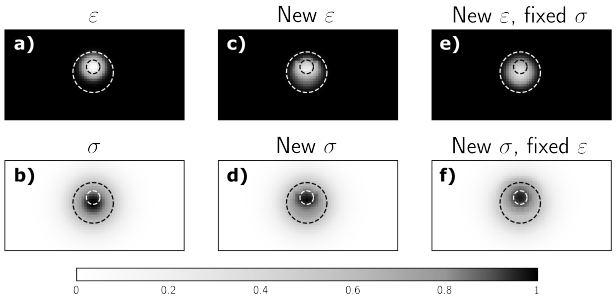

Figure 1: Illustration of cross-gradient possibilities. Given estimates $\boldsymbol{\varepsilon}$ and $\boldsymbol{\sigma}$ in **a** and **b**, Θ_τ is minimized by updating both $\boldsymbol{\varepsilon}$ and $\boldsymbol{\sigma}$ in **c** and **d**, updating $\boldsymbol{\varepsilon}$ and keeping $\boldsymbol{\sigma}$ fixed in **e**, and updating $\boldsymbol{\sigma}$ keeping $\boldsymbol{\varepsilon}$ fixed in **f**. The dashed circles are constant markers for the widths and centers of the gaussian shapes in the given estimates of $\boldsymbol{\varepsilon}$ and $\boldsymbol{\sigma}$.

where n_w and n_{dc} denote the number of sources in the GPR and ER surveys respectively. The step-sizes α_σ and α_{dc} are computed minimizing a parabolic line-search (Domenzain et al., 2019a).

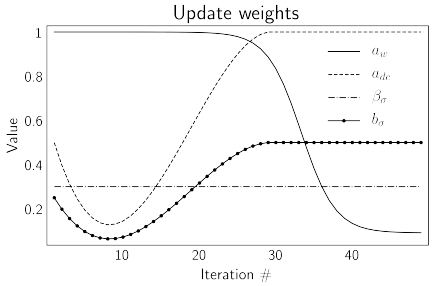

Figure 2: Qualitative optimal shape for weights throughout iterations. Because the ER data struggles to resolve the conductivity at depth in early iterations and the GPR data first resolves the structure of the model, the weight a_w is given a larger value than a_{dc} at early iterations. Once the GPR data has resolved enough structure, the roles of a_w and a_{dc} are reversed. The envelope weights β_ε and β_σ remain constant through the inversion. The cross-gradient weights b_ε and b_σ increase their contribution through out the inversion as the parameters are better resolved.

The next step is to add the updates $\Delta\boldsymbol{\sigma}_w$ and $\Delta\boldsymbol{\sigma}_{dc}$,

$$\Delta\boldsymbol{\sigma} = a_w\,\Delta\boldsymbol{\sigma}_w + a_{dc}\,\Delta\boldsymbol{\sigma}_{dc}, \tag{10}$$

where the weights a_w and a_{dc} are computed as in Domenzain et al. (2019a). See Figure 2 for a qualitative diagram.

We then normalize $\Delta\boldsymbol{\sigma}$ by its largest amplitude and write,

$$\Delta\boldsymbol{\sigma} \leftarrow c\,\Delta\boldsymbol{\sigma}, \tag{11}$$

where c is the geometric mean of the maximum amplitudes of $\Delta\boldsymbol{\sigma}_w$ and $\Delta\boldsymbol{\sigma}_{dc}$ prior to normalization.

The update to the parameters is given by,

$$\boldsymbol{\sigma} \leftarrow \boldsymbol{\sigma} \odot \exp(\boldsymbol{\sigma} \odot \Delta\boldsymbol{\sigma}), \quad (12)$$

$$\boldsymbol{\varepsilon} \leftarrow \boldsymbol{\varepsilon} \odot \exp(\boldsymbol{\varepsilon} \odot \Delta\boldsymbol{\varepsilon}), \quad (13)$$

where logarithmic values of the parameters where taken to enforce positivity constraints (Meles et al., 2010).

SYNTHETIC EXAMPLE

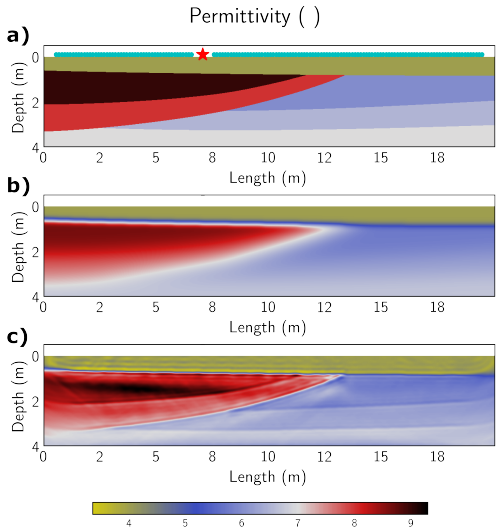

Figure 3: Permittivity values for the synthetic alluvial acquifer. True, initial and recovered models in **a, b** and **c** respectively. Source and receiver positions for a GPR shot-gather in **a**.

We test our algorithm on a synthetic model resembling an alluvial aquifer (see Figure 3**a** and Figure 4**a**). We model 20 GPR shot-gathers with a 250MHz radar Ricker pulse on a surface acquisition scenario as well as all dipole-dipole, Wenner and Schlumberger ER arrays.

The GPR source-receiver spacing is 0.5m (approximately one wavelength) with receiver-receiver distance equal to 0.125m, see Figure 3**a**. The ER electrodes are placed at 1m intervals, see Figure 4**a**. Figure 5**a** shows an example of the observed GPR shot-gather.

We choose initial models shown in Figure 3**b** and Figure 4**b**. They hold long wavelength structure that could be obtained from reflection tomography and careful analysis of direct arrivals as detailed in Bradford et al. (2009). The magnitude of the initial parameters is 4% less than the true values. In Figure 6**a** we show that although demanding, these initial models do not resolve most of the features in the model: the initial error contains most of the events present in the observed data.

Our recovered parameters are shown in Figure 3**c** and Figure 4**c**. We note the shallow reflector is now placed correclty at depth and the magnitude of the parameters in the low-velocity region are closer to the true solution in both parameters. The sharp corner of the low-velocity region (less than a wavelength wide) is resolved. The bottom reflectors are also resolved.

Figure 5**b** shows the GPR data with the recovered parameters, and Figure 6**b** shows the final error. In Figure 6**b** we see artifacts at short offsets and early times caused by having the wrong magnitude in the initial models.

CONCLUSIONS

We present a non-linear 2D multi-parameter joint inversion of GPR and electrical resistivity (ER) data that recovers electrical permittivity and conductivity of the subsurface. Our algorithm makes full use of the recorded data to compute the data sensitivities by using the adjoint method. We use the envelope transform in the full waveform inversion (FWI) scheme to enhance longer wavelength resolution and accuracy at depth of the parameters. By imposing structural constraints via cross-gradients on the parameters, we are able to weigh the structure of permittivity over conductivity or vice-versa. This enables our algorithm to inform both parameters of their missing spatial-frequency content. By calculating the GPR and ER sensitivities in the same computational grid, we directly link the GPR and ER conductivity honoring Maxwell's equations. This improves the accuracy and low frequency content of the conductivity solution, which when used with the cross-gradients constraint, also improves the permittivity solution.

Our algorithm makes no use of external regularization. However, a smooth initial model is needed for convergence to a satisfactory solution. We assume DC and effective conductivity are equal. Although this approximation is valid within an order of magnitude for most earth materials, inverting for both DC and effective conductivity is left for future work.

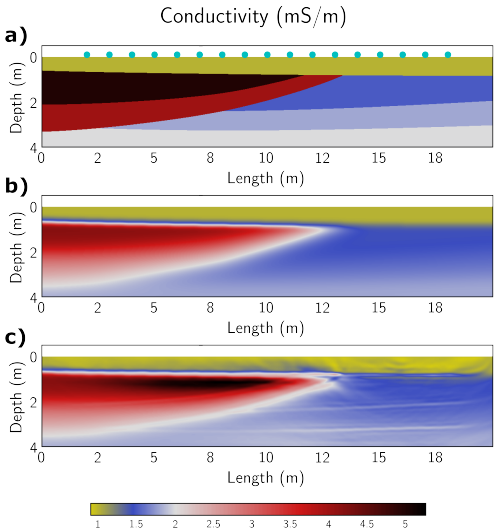

Figure 4: Conductivity values for the synthetic alluvial acquifer. True, initial and recovered models in **a, b** and **c** respectively. Electrode positions for the ER survey in **a**.

REFERENCES

Bozdağ, E., J. Trampert, and J. Tromp, 2011, Misfit functions for full waveform inversion based on instantaneous phase and envelope measurements: Geophysical Journal International, **185**, 845–870.

Bradford, J. H., 2007, Frequency-dependent attenuation analysis of ground-penetrating radar data: Geophysics, **72**, J7–J16.

Bradford, J. H., W. P. Clement, and W. Barrash, 2009, Estimating porosity with ground-penetrating radar reflection tomography: A controlled 3-d experiment at the boise hydrogeophysical research site: Water Resources Research, **45**.

Domenzain, D., J. Bradford, and J. Mead, 2018, Joint inversion of gpr and er data, *in* SEG Technical Program Expanded Abstracts 2018: Society of Exploration Geophysicists, 4763–4767.

———, 2019a, Joint inversion of full-waveform gpr and er data. part 1: In review.

———, 2019b, Joint inversion of full-waveform gpr and er data. part 2: enhancing low frequencies with the envelope transform and cross-gradients: In review.

Friel, R., and D. Or, 1999, Frequency analysis of time-domain reflectometry (tdr) with application to dielectric spectroscopy of soil constituents: Geophysics, **64**, 707–718.

Gallardo, L. A., and M. A. Meju, 2003, Characterization of heterogeneous near-surface materials by joint 2d inversion of dc resistivity and seismic data: Geophysical Research Letters, **30**.

Haber, E., and D. Oldenburg, 1997, Joint inversion: a structural approach: Inverse problems, **13**, 63.

Lavoué, F., R. Brossier, L. Métivier, S. Garambois, and J. Virieux, 2014, Two-dimensional permittivity and conductivity imaging by full waveform inversion of multioffset gpr data: A frequency-domain quasi-newton approach: Geophysical Journal International, **197**, 248–268.

Liu, Z., and J. Zhang, 2017, Joint traveltime and waveform envelope inversion for near-surface imaging: Pure and Applied Geophysics, **174**, 1269–1289.

Meles, G., S. Greenhalgh, J. Van der Kruk, A. Green, and H. Maurer, 2012, Taming the non-linearity problem in gpr full-waveform inversion for high contrast media: Journal of Applied Geophysics, **78**, 31–43.

Meles, G. A., J. Van der Kruk, S. A. Greenhalgh, J. R. Ernst, H. Maurer, and A. G. Green, 2010, A new vector waveform inversion algorithm for simultaneous updating of conductivity and permittivity parameters from combination crosshole/borehole-to-surface gpr data: IEEE Transactions on geoscience and remote sensing, **48**, 3391–3407.

Pratt, R. G., C. Shin, and G. Hick, 1998, Gauss–newton and full newton methods in frequency–space seismic waveform inversion: Geophysical Journal International, **133**, 341–362.

Taherian, M., W. Kenyon, and K. Safinya, 1990, Measurement of dielectric response of water-saturated rocks: Geophysics, **55**, 1530–1541.

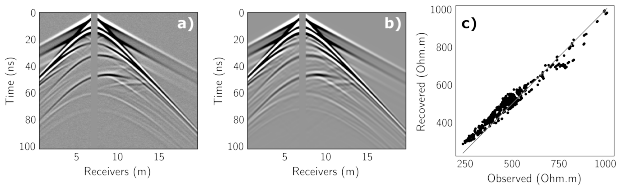

Figure 5: Example of GPR observed (**a**) and recovered (**b**) data. In **c** observed and recovered ER data.

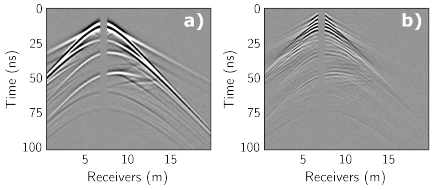

Figure 6: GPR errors of observed vs initial (**a**) and observed vs final (**b**) data. The amplitudes are clipped to 1.5% of the maximum amplitude in the data.